

The excitation mechanisms and evolutionary stages of UWISH2 planetary nebula candidates

A. M. Jones^{1*}, T. M. Gledhill¹, D. Froebrich² and M. D. Smith²

¹Centre for Astrophysics Research, University of Hertfordshire, College Lane, Hatfield AL10 9AB, UK

²Centre for Astrophysics & Planetary Science, The University of Kent, Canterbury, Kent CT2 7NH, UK

Accepted XXX. Received YYY; in original form ZZZ

ABSTRACT

We present medium-resolution K-band long-slit spectroscopy of 29 true, likely, possible and candidate Galactic Plane planetary nebulae (PNe) from the UWISH2 survey - many of which have only been recently discovered. These objects are bright in molecular hydrogen (H₂) emission, and many have bipolar morphologies. Through the detection of the Br γ emission line, which traces ionized hydrogen, we find that the majority of the candidate PNe are indeed likely to be PNe, while 2 of the targets are more likely young stellar objects (YSOs) or pre-planetary nebulae (pPNe). We detect Br γ in 13 objects which have no detection in IPHAS or SHS H α surveys. This implies they are potential members of the little-known optically-obscured PN population, hidden from wide-field optical surveys. We use the spatial extent of the H₂ 1-0 S(1) and Br γ lines to estimate the evolutionary stage of our targets, and find that W-BPNe (bipolar PNe with pinched waist morphologies) are likely to be younger objects, while R-BPNe (bipolar PNe with large ring structures) are more evolved. We use line ratios to trace the excitation mechanism of the H₂, and find the 1-0 S(1) / 2-1 S(1) and 1-0 S(1) / Br γ ratios are higher for R-BPNe, implying the H₂ is thermally excited. However, in W-BPNe, these ratios are lower, and so UV-fluorescence may be contributing to the excitation of H₂.

Key words: ISM: lines and bands – infrared: ISM – planetary nebulae: general

1 INTRODUCTION

A planetary nebula (PN, or PNe plural) is an expanding gaseous shell, formed from the material released during periods of heavy mass loss on the asymptotic giant branch (AGB) phase of stellar evolution (Paczynski 1970). It is the penultimate stage of evolution for a low to intermediate mass star (0.8 M_{\odot} to 8 M_{\odot}). The star responsible for the formation of the PN (central star, or CSPN), will move to the left of the Hertzsprung-Russell diagram as its surface temperature increases, until eventually becoming a white dwarf. UV radiation from the CSPN excites and ionizes the gaseous material, creating strong emission lines in the optical and infrared.

There are currently over 3000 PNe known in the Milky Way (Parker et al. 2016). Many of these were discovered by H α emission surveys, including the SuperCOSMOS H α Survey (SHS; Parker et al. 2005) and INT Photometric H α Survey of the Northern Galactic Plane (IPHAS; Drew et al. 2005). However it is likely that many PNe are yet to be

discovered, obscured by dust in the Galactic Plane. It is therefore necessary to switch to infrared observations, which can penetrate the dust and reveal a variety of new objects. Studies such as those of Cohen et al. (2011) and Parker et al. (2012) have shown how certain infrared diagnostics can be used in order to successfully separate PNe from possible imposters.

The near-IR region is ideal for studying molecular hydrogen (H₂) in PNe - something known to us since its first detection by Treffers et al. (1976). Many PNe contain large reservoirs of H₂ in and outside the photodissociation region (PDR) (Tielens & Hollenbach 1993), and it has also been proposed that H₂ emission can originate from the ionized region (Aleman & Gruenwald 2011). However, extended H₂ emission can also be detected at large distances from the main nebula site, as shown recently by Fang et al. (2018). H₂ is therefore an excellent tracer of the morphology of PNe, and many studies have been conducted to investigate relationships between morphology and H₂ emission. For example, there is strong observational evidence that bipolar PNe (BPNe) have brighter H₂ emission - known as Gately's Rule (Zuckerman & Gately 1988; Kastner et al. 1994). How-

* E-mail: aj16acd@herts.ac.uk

Table 1. Observation log and additional information for the 29 targets. Morphologies and sizes in H_2 and $H\alpha$ are taken from table A1 of Gledhill et al. (2018). Morphologies make use of the ‘ERBIAS’ classification system (Parker et al. 2006), and sizes are the major and minor axis dimensions in arcsec. Where no $H\alpha$ morphology is given, the object is not detected in $H\alpha$ emission. PN status comes from the HASH PN database (Parker et al. 2016), where ‘T’, ‘L’, ‘P’ and ‘C’ refer to true, likely, possible and candidate PNe - see text for details.

PN G	Other names	RA	Dec	Integration (s)	Airmass	H_2		$H\alpha$		PN status
						Morph.	Size	Morph.	Size	
004.7-00.8	—	269.95542	-25.26527	1200	1.71	Bams	25x12	—	—	C
009.7-00.9	SSTGLMC G009.7612-00.9575	272.71231	-20.96230	1200	1.56	Bs	18x6	—	—	C
020.7-00.1	—	277.37398	-10.94099	1200	1.46	Bs	14x9	A	15x9	C
020.8+00.4	SSTGLMC G020.8543+00.4857	276.84922	-10.50625	1200	1.34	B	2.8x1.2	—	—	C
024.8+00.4	SSTGLMC G024.8959+00.4586	278.76581	-6.93617	1200	1.23	Bs	14x6	—	—	C
025.9-00.5	—	280.21143	-6.44546	1200	1.46	Ers	8x5	—	—	C
032.6-01.2	MPA J1855-0048	283.85720	-0.80638	1200	1.31	Bps	12x5	E	10x5	T
034.8+01.3	—	282.55901	+2.30305	1200	1.17	Bs	14x7	—	—	C
035.7-01.2	NVSS 190102+015727	285.26293	+1.95644	1200	1.17	Bs	26x12	—	—	C
036.4+00.1	GPSR5 36.481+0.155	284.34075	+3.23021	1200	1.25	Bps	12x5	—	—	C
037.4-00.1	—	285.07885	+3.90133	1080	1.28	Er	6x5	—	—	C
040.4+01.1	—	285.32726	+7.20967	1200	1.11	Bs	12x4	—	—	C
040.5-00.7	—	287.02679	+6.41554	1200	1.24	Bs	12x7	—	—	C
042.1+00.4	—	286.67062	+8.38580	1200	1.55	Bs	9x9	—	—	C
047.1+00.4	—	289.05872	+12.86745	1200	1.27	Brs	25x14	S?	—	C
047.5-00.3	—	289.95370	+12.76896	1200	1.24	Es	12x8	—	—	C
048.2-00.4	—	290.40474	+13.37742	1200	1.47	Bs	10x8	—	—	C
050.0-00.7	—	291.57894	+14.80423	1320	1.41	Bs	12x12	—	—	C
050.5+00.0	NVSS J192414+153909	291.06046	+15.65315	1320	1.23	Bs	16x5	S	—	L
057.9-00.7	Kn 7	295.60822	+21.75634	1080	1.33	Brs	26x20	B	27x30	T
058.1-00.8	IPHASX J194301.3+215424	295.75604	+21.90672	1320	1.61	Bs	20x12	B	15x12	L
059.7-00.8	IPHASX J194633.0+231659	296.63714	+23.28371	1440	1.17	Bs	12x9	Ea	13x9	P
060.5-00.3	K 3-45	296.56513	+24.18437	1200	1.93	Bps	11x6	Bs	11x6	T
061.8+00.8	—	296.14467	+25.92826	1200	1.40	Bs	12x13	B?	12x12	C
062.1+00.1	—	297.01712	+25.81331	1200	1.71	Ear	12x10	E?	10x8	C
062.2+01.1	—	296.15164	+26.44203	1200	1.00	Bs	16x10	E?	11	C
062.7+00.0	IPHASX J194940.9+261521	297.42017	+26.25520	1200	2.20	Bs	17x8	Bps	13x7	T
064.1+00.7	—	297.57807	+27.89812	1080	1.05	Bs	11x4.5	E?	2.3x4	C
064.9+00.7	—	298.03161	+28.54425	1200	1.96	Brs	10x8	B?	10x8.5	C

ever, H_2 can also be detected in ellipsoidal or barrel-like PNe (Marquez-Lugo et al. 2013). Bipolar PNe can be further divided into those showing broad, ring-like features (R-BPNe) and those with narrow waists or compact centres (W-BPNe) (Manchado et al. 1996). The nature of this divide is uncertain - they may form an evolutionary sequence, or originate from different progenitor populations (Guerrero et al. 2000).

The K-band (2 - 2.4 μm) is home to a wide range of ro-vibrational lines of H_2 , including the $v = 1-0$ S(1) (2.1218 μm) and 2-1 S(1) (2.2477 μm) lines. Ratios of these lines can indicate the mechanisms responsible for the excitation of the H_2 (Black & Dalgarno 1976). Also in this waveband lie recombination lines of hydrogen and helium. The detection of the Bry H recombination line at 2.1661 μm signifies that the CSPN has begun to photoionize its environment, however this line can also be produced in shocks. Imaging of this line is a powerful tool for studying the evolution of PNe, especially in the transition from proto-planetary nebulae (pPNe) to PNe (Gledhill & Forde 2015). The presence of these emission lines makes the K-band particularly advantageous to study both the molecular and ionized components of PNe.

In this work, we present K-band long-slit spectra of a sample of PNe and candidate PNe taken from the recent UWISH2 imaging survey (UKIRT Widefield Infrared Survey for H_2) (Froeblich et al. 2011). We focus on the mechanisms governing the excitation of H_2 , and how these relate to the evolutionary stages and morphologies of the targets. Along with spectra, we make use of near-IR H_2 and optical $H\alpha$ imaging, and mid-IR colours where available. In Sect. 2, we

describe the sample and the available data. Sect. 3 outlines our observations, and methods used to reduce the data. In Sect. 4 we describe the spectra and images of the objects, and discuss the links between morphology, line ratios and evolution in Sect. 5. Finally, we make our conclusions in Sect. 6.

2 SAMPLE

UWISH2 was an unbiased Galactic Plane survey, focussed on the H_2 1-0 S(1) line at 2.1218 μm . A total of 284 candidate PNe were found to lie in its survey area, including those already known to us, and many new discoveries with no known optical counterparts (Froeblich et al. 2015). Gledhill et al. (2018), hereafter G18, have since updated this number to 291 candidates. Our sample for spectroscopic follow-up consisted of 29 targets, selected mainly due to their bright H_2 fluxes. The objects lie at low Galactic latitudes ($-1.5^\circ < b < 1.5^\circ$) and have longitudes in the range ($0^\circ < l < 65^\circ$). Table 1 lists all the targets observed.

Four of our targets have a PN status of ‘true’, and have been confirmed as PNe through available multi-wavelength data. Two have the status ‘likely’, for objects that are likely to be PNe but do not have completely conclusive morphology/spectroscopy data. One is labelled ‘possible’, indicating a possible PN with currently insufficient data. The remaining 22 targets have the status ‘new candidate’ - these have been classified as candidate PNe by the UWISH2 survey on the basis of morphology and lack of association with known

star-forming regions. These statuses come from the HASH PN database¹ (Parker et al. 2016). H α images are available for all 29 targets, however only 14 show evidence of H α emission, with 7 of these having been previously reported.

It is also apparent that some of our targets are bright in the mid-IR, with Spitzer/IRAC imaging available at 3.6, 4.5, 5.8, and 8.0 μm from the GLIMPSE survey². Mid-IR colour-colour plots can be used as an additional diagnostic to imaging and spectroscopy, to distinguish PNe from possible mimics, as their various infrared properties cause them to populate different regions of the diagrams (e.g. Robitaille et al. 2008; Cohen et al. 2011). G18 have measured IRAC colours for targets in the UWISH2 survey with detectable mid-IR emission, which includes the targets from this work. Fluxes in all four bands are available for 18 of the targets.

3 OBSERVATIONS AND DATA REDUCTION

Observations were obtained on the 22nd - 24th July, 2016, using the Long-slit Intermediate Resolution Infrared Spectrograph (LIRIS: Manchado et al. 2003; Acosta Pulido et al. 2003) on the William Herschel Telescope (WHT), located at the Observatorio del Roque de los Muchachos on La Palma, Canary Islands. LIRIS uses a 1024×1024 HAWAII detector, with a pixel scale of $0.25 \text{ arcsec pixel}^{-1}$, yielding a field of view of $4.27 \text{ arcmin} \times 4.27 \text{ arcmin}$.

We used a slit width of 1 arcsec for the brighter targets, and increased it to 2.5 arcsec for the fainter ones. The slit was generally oriented along the major axis of the nebula, as defined by UWISH2 images, or to contain the brightest H $_2$ features. However, this sometimes led to nearby stars falling within the slit, rendering certain sections of the data unusable. The extraction sections are marked on the UWISH2 H $_2$ - K images in Fig. A1, along with Fig. 1a for PN G050.5+00.0, which includes the K band continuum, and Fig. 2a for PN G059.7-00.8. Table 1 gives observational details for each target.

Standard stars with spectral types B8 to A3 were observed throughout the 3 nights, as their spectra in the K-band are relatively featureless, apart from absorption at Bry, which needed to be removed. Both the targets and standards were observed in a A-B-B-A nodding sequence, in order to effectively subtract the sky contribution. After flat-field correction, the images were aligned and stacked to form two-dimensional spectra with an increased signal to noise, which were then extracted at various positions along the slit to form multiple one-dimensional spectra. Arc images were used to wavelength calibrate the spectra, giving a spectral resolution of $\approx 3.6 \text{ \AA pixel}^{-1}$. This was followed by telluric correction and flux calibration using the standard star spectra. Standard IRAF routines (Tody 1993) were used for flat-field correction, wavelength calibration, telluric correction, flux calibration and image combination. PYTHON with the ASTROPY module (Astropy Collaboration et al. 2013) was used to extract the spectra. In order to calculate emission line fluxes, Gaussians were fitted to the spectra using the CURVE FIT function from the PYTHON SCIPY module (Jones

et al. 2001), which uses non-linear least squares in order to fit a function to the data.

We also obtained narrow-band imaging of PNG050.5+00.0, using LIRIS. The observations were carried out on the 26th September, 2017, using the Bry and K-band continuum filters, which included flatfield frames. The average airmass of the target frames was 1.33, with a seeing of $\approx 1 \text{ arcsec}$. Images were taken at 5 noddings - stacking the unaligned images together created a sky frame, which was subtracted from each target frame to remove the sky contribution. These were then aligned and stacked to form the final image. Standard IRAF routines were used in flatfielding, image alignment and stacking. In order to highlight any structures within the bright central region of PNG050.5+00.0, we deconvolved the image using the Richardson-Lucy algorithm (Richardson 1972; Lucy 1974). This was achieved using a star within the same field to act as a point spread function, in order to improve the resolution. The procedure was carried out using the LUCY routine in the STARLINK package KAPPA (Currie et al. 2014).

4 RESULTS

Figures 1d and 1e for PNG050.5+00.0, 2b and 2c for PNG059.7-00.8, and Fig. B1 for the remaining targets, show the fully calibrated emission spectra, with identified features labelled. All targets have the $v = 1-0 \text{ S}(1)$, $1-0 \text{ S}(0)$ and $1-0 \text{ Q}(1)$ H $_2$ emission lines, albeit the latter line is often weak due to poor atmospheric transmission. Higher vibrational level H $_2$ lines are identified in some objects, including the $3-2 \text{ S}(2)$ and $3-2 \text{ S}(3)$ lines. Bry ($2.1661 \mu\text{m}$) is seen in all but 4 objects³, signifying the presence of ionized hydrogen. We detect the He I ($2.0587 \mu\text{m}$) line in 9 targets, which means their central stars have become hot enough that their UV photons are capable of ionizing He. We also see the weaker He I ($2.1127 \mu\text{m}$) line in 3 targets, and the He II ($2.1891 \mu\text{m}$) line in 4 targets. These, and a range of other H $_2$ emission lines seen in our targets are listed in Table C1, along with their fluxes.

4.1 PN G050.5+00.0

PN G050.5+00.0 is a particularly interesting object, with a range of radio data available. It has been classified as a ‘likely PN’, (e.g. the CORNISH 5.0 GHz survey; Hoare et al. 2012; and the RMS survey; Urquhart et al. 2009), while the Green Bank Telescope (GBT) H II Region Discovery Survey (Anderson et al. 2011) classifies PN G050.5+00.0 as a H II region. The UWISH2 image is shown in Fig. 1a, without K-band subtraction⁴. PN G050.5+00.0 has a cigar-shaped H $_2$ morphology, surrounded by a rim of stronger emission.

³ We do not detect Bry in PN G062.1+00.1 or 064.9+00.7, however these objects have clear H α emission in their IPHAS images. We attribute this lack of detection to a combination of high airmass during observations, and nearby stars preventing extraction of the central regions, where the H $^+$ is thought to be concentrated.

⁴ We include the H $_2$ image to give a better view of the central region, as the H $_2$ - K image of the centre is dominated by negative flux, due to a strong Bry flux in the K-band leading to an over-subtraction.

¹ <http://hashpn.space>

² http://irsa.ipac.caltech.edu/data/SPITZER/GLIMPSE/index_cutouts.html

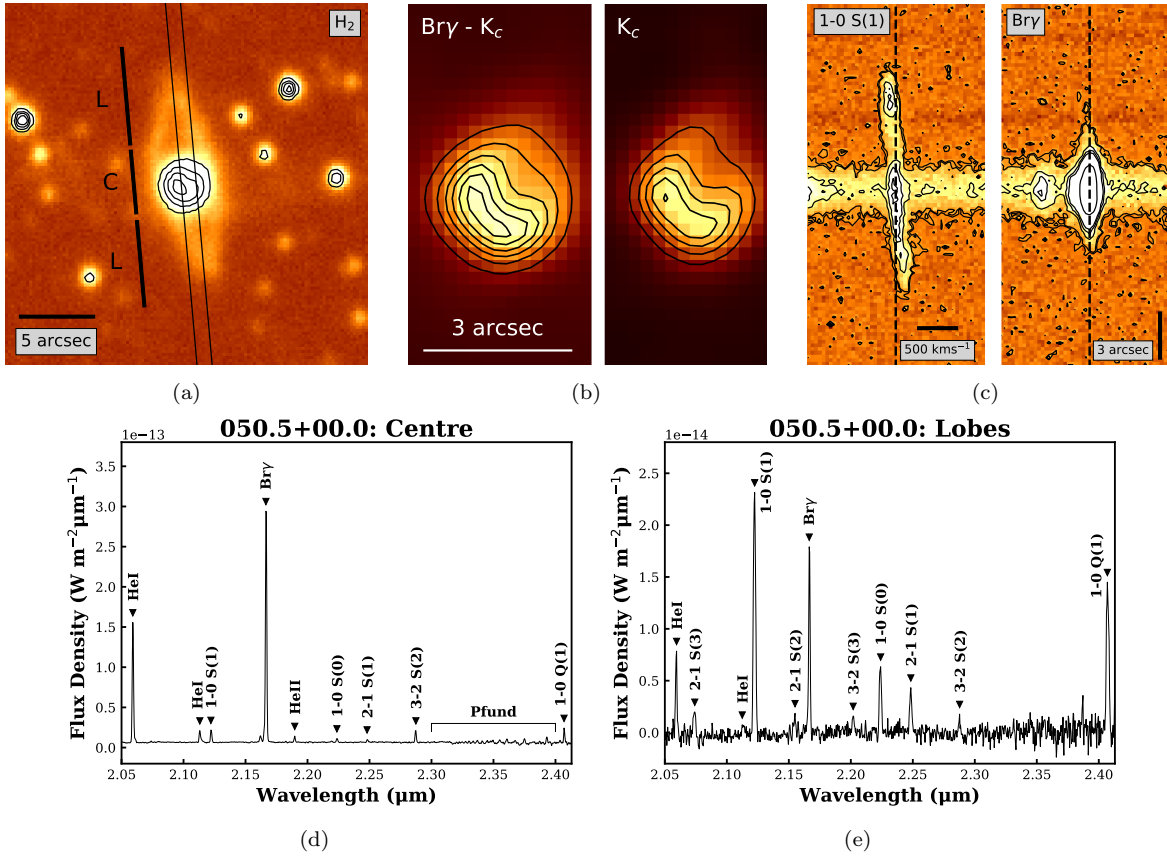


Figure 1. K-band images and spectra for PN G050.5+00.0. a) H₂ image from UWISH2, showing position and width of slit, and extraction sections. Contours range from 2400 to 3600 counts, in steps of 400. b) Deconvolved narrow-band Bry - K_c (left) and K_c continuum (right) images of the central region. Contours range from 500 to 3000 counts, in steps of 500. c) Two-dimensional spectra for the 1-0 S(1) and Bry lines, with dotted lines drawn through their centres. d) K-band spectrum of central region e) K-band spectrum of the sum of the lobes.

The object has a very bright central region, which is likely a combination of H₂ and K-band continuum emission (K_c). We also find strong Bry emission here, which extends slightly into the lobes where there is a void of H₂; more noticeable in the northern lobe (Fig. 1c).

We overlay contours on Fig. 1a to highlight structure in the centre. We find the emission here is not uniform, but instead peaks at a point slightly to the southeast. This encouraged us to attempt narrow band Bry and K_c imaging, to see if it would be possible to further resolve the central region, and to investigate the structure of the ionized and continuum emission. We show the deconvolved Bry - K_c, and K_c images in (Fig. 1b). Both have elongated structures, slightly offset from the centre of the object, which are similar to the structure seen in Fig. 1a. This leads us to believe that the Bry and continuum emission both originate from the unresolved central region, and are being scattered by the same spatially extended dusty structure.

Higher vibrational level H₂ lines, and recombination lines of helium (including those of He I and He II) are seen in the spectra of PN G050.5+00.0 (Figures 1d and 1e). The Pfund series is also visible in the spectrum of the central region, from 2.3 μm onwards. In the two-dimensional spectrum of PN G050.5+00.0, we find the H₂ emission lines are slanted, indicating that the northern lobe is blueshifted, while the southern lobe is redshifted. We suggest two possi-

ble scenarios - either the object has curved outflows (where the northern lobe curves towards us, while the southern lobe curves away), or the outflows are accelerating. We show a region of the two-dimensional spectrum, centred on the 1-0 S(1) line, in Fig. 1c, which is essentially a position-velocity diagram. We measure the wavelength shift from the centre to the end of each lobe to be $7.2 \pm 3.6 \text{ \AA}$, which gives a line-of-sight velocity of $100 \pm 50 \text{ km s}^{-1}$, relative to the systemic velocity. This is a lower limit on the expansion velocity, as any inclination to the line-of-sight will act to raise this value. Mid-IR colours measured by G18 suggest that PN G050.5+00.0 is more likely to be a PN rather than a H II region.

4.2 PN G059.7-00.8

PN G059.7-00.8 is a ‘possible’ PN, with an optical spectrum and imaging available⁵. The object has a steady rising continuum in the optical (4000 to 8000 Å), with strong emission lines of [O III], [N II] and H α . It has an elliptical morphology in H α emission, however its H₂ structure is spider-like, with stronger shells of emission to the northeast and southwest (Fig 2a). In the centre of PN G059.7-00.8, we find a very

⁵ These can be found on the HASH PN database.

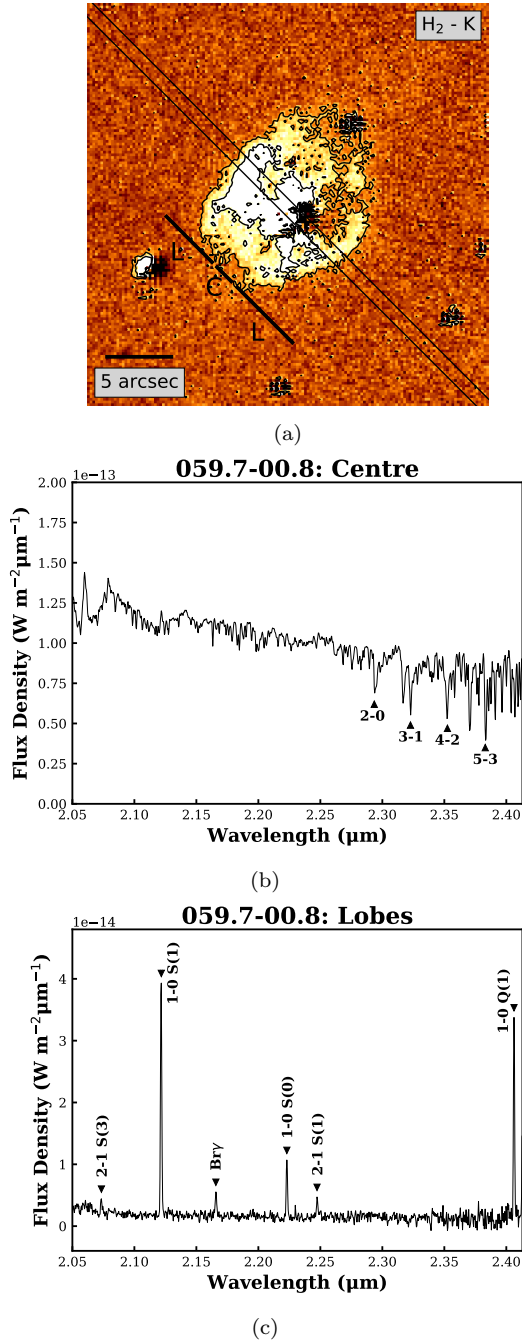


Figure 2. K-band image and spectra for PN G059.7-00.8. a) H₂ - K image from UWISH2, showing position and width of slit, and extraction sections. Contours are located at 50 and 150 counts. b) K-band spectrum of central region, with CO bandheads labelled c) K-band spectrum of the sum of the lobes.

bright source, and investigate to see if it is related to the object. The spectrum of this source, with a bright continuum, is shown in Fig. 2b. The continuum falls at longer wavelengths, and we find multiple CO bandheads in absorption, including the $v = 2-0$ (2.2935 μm), 3-1 (2.3227 μm), 4-2 (2.3535 μm) and 5-3 (2.3829 μm). These are characteristics common among YSOs (Casali & Eiroa 1996; Reipurth & Aspin 1997) but are also present in main sequence dwarf stars of spectral type K and later. The nebula spectrum at optical

wavelengths shows emission lines typical of a PN, plus G18 measure mid-IR colours consistent with a PN. We suspect, therefore, that the bright central source is an unrelated field star projected onto the PN.

4.3 Candidate PNe

22 targets in our sample are candidate PNe selected by the UWISH2 survey, with the remaining 7 targets either true, likely or possible PNe. 7 of the candidates have H α emission in either IPHAS or SHS images (see Table 1). 13 candidate PNe have the Bry line, but show no signs of H α emission in optical surveys. These are likely to be members of the optically-obscured PN population. Two of the candidates, PNG004.7-00.8 and PNG020.8+00.4, show no signs of Bry or H α emission - a lack of H⁺ suggests these may not be PNe. Both objects have bipolar morphologies, however the former has multiple extended structures, including a large sweeping tail of H₂ extending eastward before turning south, while the latter consists of two small blobs of H₂ emission. G18 find mid-IR colours which place PNG004.7-00.8 in the YSO region, while the mid-IR colours of PNG020.8+00.4 are not consistent with PNe, YSOs or H II regions; instead it seems more likely to be a proto-planetary nebula (pPN).

We classified 4 of the candidates as W-BPNe, including PNG009.7-00.9, G024.8+00.4, G036.4+00.1 and G040.4+01.1. These objects have either a compact core or a narrow, pinched waist in H₂ emission. All of these have strong Bry and He I (2.0587 μm) lines in their central regions, while the first two have $v = 3-2$ H₂ lines and additional helium lines (He I at 2.1127 μm and He II at 2.1891 μm) in their spectra. None show evidence of H α emission, implying strong line-of-sight extinction. The cores of PNG009.7-00.9 and G036.4+00.1 can be resolved into two knots of H₂, which could be signs of molecular tori being viewed side-on (Kerber & Claeskens 1997). PNG024.8+00.4 has well-separated H₂ lobes, with a smaller knot of emission just south of the centre. Its spectrum has a continuum gradually rising with wavelength, which is often a sign of dust. PNG040.4+01.1 also has two separated lobes, with two smaller knots to the northwest and southeast of the centre, which again could be due to a molecular torus.

Most of the remaining candidates we consider to be R-BPNe, which are bipolars with equatorial ring structures⁶, with the exception of PNG025.9-00.5, G037.4-00.1 and G047.5-00.34, whose H₂ morphologies are more elliptical. The R-BPNe in our sample have fairly similar spectra which lack the $v = 3-2$ H₂ lines. The He I (2.0587 μm) line is observed in 3 of these objects, and one of the elliptical PNe (PNG037.4-00.1). The most impressive of the R-BPNe is PNG035.7-01.2, with the largest angular size of the sample. The object has arcs of H₂, which are likely to be cavity walls. It is invisible in H α , but Bry lines are present in our spectra. PNG047.1+00.4 also has an interesting morphology, which is point-symmetric resembling an eye rotated by 90°. It has a ring of H₂ emission, and two curved arms extending in the north and south directions. Spectra and H α images reveal

⁶ It is sometimes difficult to see a clear ring feature, however we label any bipolar objects as R-BPNe if their morphology is obviously not of the W-BPN or elliptical type.

an ionized region localised to the centre, where we also observe the He II (2.1891 μm) line - this is the only R-BPN in our sample which shows this feature. However, this could be an orientation effect, where we are looking down the major axis of the object, and from another viewing angle, the object could look more like a W-BPN.

5 DISCUSSION

A simple means of determining the evolutionary stage of a PN is to observe the spatial extent of ionized material, traced by Bry emission, in relation to the extent of H₂ emission. It follows that in pPNe, Bry emission should be absent, as their central stars are not yet hot enough to ionize the surrounding envelope. When the temperature reaches ≈ 25000 K, ionization produces Bry emission localised to the central region. As the PN evolves, the ionization front moves outwards, gradually replacing the molecular material. This process can be clearly seen in young PNe (Gledhill & Forde 2015). As not all of our targets are visible at H α , we can use the two-dimensional spectra to measure the radius of the ionized region along the slit using the Bry emission, which can then be compared to the radius of H₂ 1-0 S(1) emission. In Fig. 3, we demonstrate how the ionized and molecular radii are estimated using this technique for two objects, PN G024.8+00.4 (left) and PN G032.6-01.2 (right). The position along the slit is given on the x-axis, and the flux (summed over the slit width) is on the y-axis. The flux of the molecular and ionized hydrogen emission lines along the slit are given by the black and red lines respectively. The point at which the flux reaches the noise level is the maximum extent of the emission line, and therefore the radius, where the shaded areas show the regions where the radii are estimated to lie. For the two objects in Fig. 3, we estimate the ratio of the diameters (or equivalently the radii) of the Bry and 1-0 S(1) lines to be 0.2 ± 0.07 and 0.75 ± 0.18 for PN G024.8+00.4 and PN G032.6-01.2 respectively. We plot the ratio of the ionized to molecular radius on the x-axis of Fig. 4a for the bipolar objects in our sample. Error bars on these values reflect the regions in which the radii are estimated to lie, as the exact point at which the emission reaches the background level when using plots such as Fig. 3 is not always clear. This is certainly the case when the signal to noise ratio is low, or when nearby stars contaminate the two-dimensional spectra. In cases where it was deemed too difficult to estimate a radius using this technique alone, H₂ and H α imaging were also inspected when available.

We separate the objects in Fig. 4a according to their bipolar type, with W-BPNe (compact core or narrow waist) in red and the R-BPNe (broad ring structures) in blue. We classify five of our targets as W-BPNe, including PN G009.7-00.9, G024.8+00.4, G036.4+00.1, G040.4+01.1 and G050.5+00.0. Most of the remaining sample we classify as R-BPNe. Three of the W-BPNe have ionized regions localised to their centres, so they are positioned to the very left of the figure. These values are upper limits, indicated by hollow arrows, as their Bry extents match the average seeing of the observations, given by the width of stellar continua in the same field of view. Fig. 3a, for PN G024.8+00.4, clearly shows the small angular extent of the Bry emission when compared to the much more extended 1-0 S(1) emis-

sion. PN G050.5+00.0 lies to the right of this group, however we showed in Sec 4.1 that this object's Bry emission is likely to be generated in an unresolved central region, and then scattered, possibly by a dusty torus, which increases its apparent Bry extent. If this scattering process were not occurring, PN G050.5+00.0 would move to the left, which we indicate by a solid arrow in Fig. 4a. PN G036.4+00.1 lies to the right of PN G050.5+00.0, however we note the slit was not positioned along the major axis of the nebula, which we believe to run northeast to southwest. Therefore, we have no information as to what extent the ionization front has travelled into the lobes. We believe if the slit were positioned along the major axis, the Bry to H₂ radius would decrease, and so we mark this object with a solid arrow to show it could also move to the left.

Once these considerations are taken into account, Fig. 4a shows a clear divide between the two morphological types, where the W-BPNe have a smaller ratio of Bry to H₂ radius, and so are less evolved, while the R-BPNe have larger Bry to H₂ radii and are therefore more evolved. Fig. 3b compares the extents of the ionized and molecular emission for an R-BPN (PN G032.6-01.2), and it can be seen these are comparable. This idea makes sense, considering that many pPNe, in the stage of evolution immediately before the PN phase, have morphologies closely resembling those of W-BPNe. It is also known that strong emission lines of He I (2.0587 μm) and Bry are seen in young PNe (Gledhill & Forde 2015), which is what we observe. On the other hand, the fact that the ionization front in the R-BPNe has moved further from the central region approaching the outer bound of the H₂ radius, means that R-BPNe have had more time to form broad, ring-like structures. Ramos-Larios et al. (2017) measure physical sizes, kinematic ages and luminosities of a sample of bipolar PNe, and also find that R-BPNe are more evolved than W-BPNe.

Information about how the H₂ is being excited can be found by comparing the fluxes of emission lines. These line ratios have the advantage that the effect of differential extinction on their values is relatively small, due to small wavelength separations between lines. H₂ can be excited thermally (e.g. in shocks) or non-thermally (e.g. UV-fluorescence). In the thermal process, H₂ molecules are collisionally heated to a few thousand degrees, and radiate near-IR photons as they cool (Burton 1987). In the non-thermal process, a H₂ molecule is excited when it absorbs a UV photon, and quickly decays to a vibrationally-excited level of the electronic ground state. Further decays result in the emission of infrared photons (Black & Dalgarno 1976). A mixture of these processes contribute to the emission lines we observe in our spectra. However, thermal processes populate the H₂ levels from the lowest ($v = 0$) to the highest ($v \geq 2$) states, whereas non-thermal processes populate from the top ($v \geq 3$) down. Therefore, ratios such as the 1-0 S(1) / 2-1 S(1) and 1-0 S(1) / 3-2 S(3) will have typical values depending on the excitation environment. A purely UV pumped spectrum will have a 1-0 S(1) / 2-1 S(1) ratio equal to 1.8 (Black & Dalgarno 1976, Black & van Dishoeck 1987), while in the thermal case, indicative of shocks, this ratio will be at least 10 (Hollenbach & Shull 1977, Burton et al. 1992). We present key line ratios in Table 2.

On the y-axis of Fig. 4a we plot the 1-0 S(1) / 2-1 S(1) ratio, summed over the object, and again there is good evi-

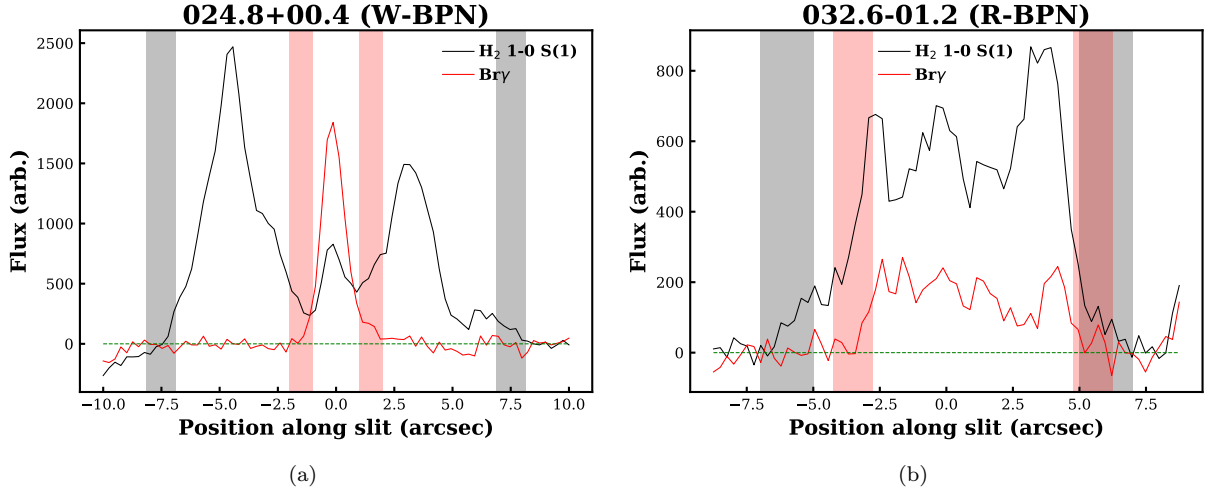


Figure 3. Slices showing the variation of the flux along the slit for PN G024.8+00.4 (a) and PN G032.6-01.2 (b), where the black and red lines are for the 1-0 S(1) and Bry hydrogen emission lines respectively. The shaded regions represent the regions where the radii are estimated to lie. The green dotted line represents zero flux.

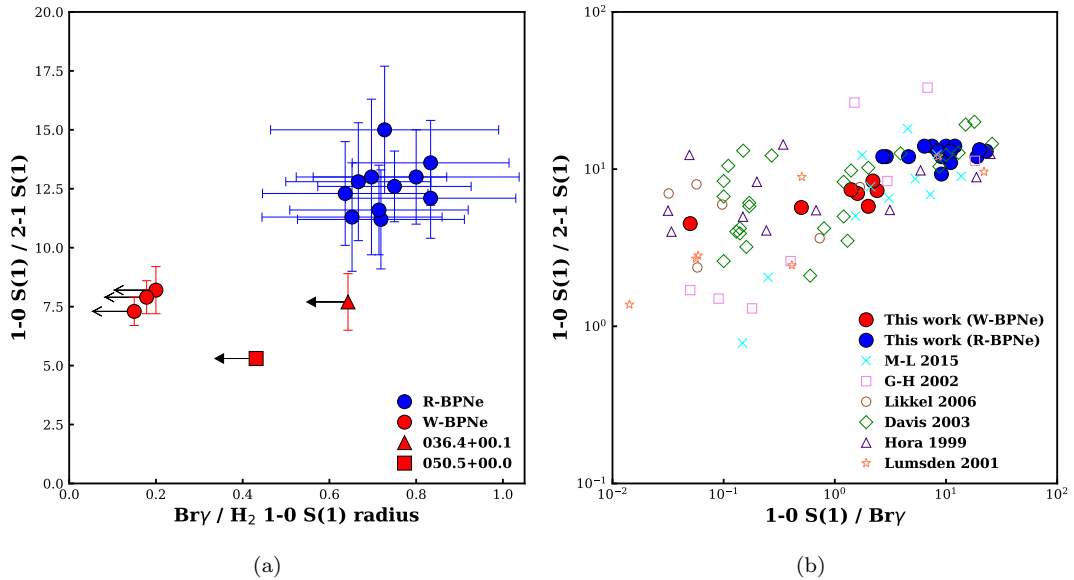


Figure 4. a) Ionized to molecular radius ratio versus 1-0 S(1) / 2-1 S(1) ratio for bipolar PNe. Error bars for radii are estimated from two-dimensional spectra. We mark solid arrows (not to scale) on two objects as we believe these should move to the left of the diagram, and hollow arrows on objects thought to represent upper limits (see text for details) b) Line ratio plot with data from this work overlaid onto previous results. This includes the individual ratios extracted at different positions along the slit.

dence for a dichotomy between the two bipolar types. Using Fig. 4a, the mean 1-0 S(1) / 2-1 S(1) ratios for the W-BPNe and R-BPNe are 7.3 ± 1.0 and 12.6 ± 1.1 respectively. This leads us to believe that on average, thermal excitation is the main mechanism exciting H₂ in R-BPNe, while the lower ratios of W-BPNe, and the fact that we only observe $v = 3-2$ H₂ transitions in these objects, could mean that UV-fluorescence plays a more important role in their excitation. While a mean 1-0 S(1) / 2-1 S(1) ratio of 7.3 is higher than the theoretical value for a purely UV pumped spectrum, a fluoresced dense gas ($n \geq 10^5 \text{ cm}^{-3}$) subjected to intense UV radiation will have an increased 1-0 S(1) / 2-1 S(1) ratio due to collisional heating (Sternberg & Dalgarno 1989, Hollenbach & Natta 1995). Further observational evidence is pro-

vided by Marquez-Lugo et al. (2015), who find UV excitation is likely occurring in the cores of W-BPNe, while R-BPNe are dominated by shock excitation. If R-BPNe are more evolved than W-BPNe, then it follows that UV-fluorescence is a process associated with younger objects, while thermal excitation prevails as the PN evolves; a trend found observationally by Davis et al. (2003). This broadly agrees with the theoretical work of Natta & Hollenbach (1998), however once high resolution integral field spectroscopy is obtained, it is evident that line ratios, and therefore excitation mechanisms, can vary across the surface of young PNe, and highlights the importance of the dependence of line ratios on density (Gledhill & Forde 2015). This is to be explored further in subsequent modelling papers.

Table 2. Key line flux ratios and errors, uncorrected for extinction. The regions of the objects these fluxes have been extracted from are shown in Appendix A1.

ID	Region	1-0 S(1) / 2-1 S(1)	1-0 S(1) / 3-2 S(3)	1-0 S(1) / Bry	He I (2.0587 μ m) / Bry
004.7-00.8	Centre	12 \pm 2	—	—	—
009.7-00.9	Centre	7.3 \pm 0.6	54 \pm 19	2.4 \pm 0.1	0.58 \pm 0.04
	Lobes	7.2 \pm 0.7	25 \pm 7	—	—
020.7-00.1	Centre	—	—	6.4 \pm 1.5	—
	Lobes	12 \pm 2	—	19 \pm 6	—
020.8+00.4	Centre	7.1 \pm 1.3	—	—	—
	Lobes	6.3 \pm 1.0	—	—	—
024.8+00.4	Centre	5.7 \pm 2.0	—	0.50 \pm 0.07	0.67 \pm 0.03
	Lobes	8.6 \pm 1.0	43 \pm 9	—	—
025.9-00.5	North lobe	—	—	11 \pm 4	—
032.6-01.2	Centre	12 \pm 2	—	2.9 \pm 0.2	0.30 \pm 0.05
	Lobes	14 \pm 2	—	7.5 \pm 0.8	—
034.8+01.3	Centre	—	—	3.4 \pm 0.4	0.25 \pm 0.08
	Lobes	11 \pm 2	—	11 \pm 1	0.48 \pm 0.14
035.7-01.2	Centre	—	—	6.4 \pm 1.3	—
	Lobes	12 \pm 2	—	9.1 \pm 1.1	—
036.4+00.1	Centre	7.0 \pm 1.5	—	1.6 \pm 0.1	0.34 \pm 0.06
	South lobe	8.4 \pm 1.7	—	2.2 \pm 0.2	0.31 \pm 0.04
037.4-00.1	Centre	6.3 \pm 1.7	—	0.44 \pm 0.07	0.28 \pm 0.07
	Lobes	9.3 \pm 1.7	—	3.7 \pm 0.4	0.28 \pm 0.0
040.4+01.1	Centre	7.4 \pm 2.5	—	1.4 \pm 0.1	0.50 \pm 0.10
	Lobes	7.8 \pm 0.7	—	—	—
040.5-00.7	All	—	—	9.8 \pm 3.7	—
042.1+00.4	All	—	—	12 \pm 2	—
047.1+00.4	Centre	—	—	0.59 \pm 0.03	0.46 \pm 0.06
	Lobes	—	—	9.2 \pm 2.6	—
047.5-00.3	All	—	—	5.5 \pm 0.7	—
048.2-00.4	All	—	—	12 \pm 3	—
050.0-00.7	Centre	—	—	6.0 \pm 1.5	—
	Lobes	—	—	—	—
050.5+00.0	Centre	4.5 \pm 0.4	—	0.05 \pm 0.01	0.49 \pm 0.01
	Lobes	5.8 \pm 0.4	16 \pm 3	2.0 \pm 0.1	0.43 \pm 0.04
057.9-00.7	Centre	14 \pm 4	—	6.4 \pm 0.7	—
	Lobes	13 \pm 1	—	23 \pm 7	—
058.1-00.8	Centre	—	—	7.9 \pm 3.2	—
	Lobes	14 \pm 4	—	10 \pm 3	—
059.7-00.8	Lobes	13 \pm 2	—	8.5 \pm 1.0	—
060.5-00.3	Centre	12 \pm 2	—	4.6 \pm 0.3	—
	Lobes	14 \pm 5	—	12 \pm 3	—
061.8+00.8	Centre	—	—	7.0 \pm 1.2	—
	Lobes	13 \pm 2	—	11 \pm 3	—
062.1+00.1	North lobe	—	—	—	—
062.2+01.1	Centre	—	—	12 \pm 3	—
	Lobes	—	—	—	—
062.7+00.0	Centre	12 \pm 3	—	2.7 \pm 0.3	—
	North lobe	—	—	6.3 \pm 1.0	—
064.1+00.7	Centre	9.3 \pm 1.8	—	9.1 \pm 1.6	—
	Lobes	13.3 \pm 3.7	—	20 \pm 5	—
064.9+00.7	Lobes	—	—	—	—

There are also indications that the 1-0 S(1) / Bry ratio is linked with the evolutionary stage, for example [Guerero et al. \(2000\)](#) find this ratio is low for young PNe, while more evolved objects have larger ratios. This is supported by G18, who find that for a small sample of 23 PNe covering a range in physical radii of 0.03 to 0.6 pc, the average H₂ surface brightness is approximately independent of size, and therefore age. Combining this with the fact that the average H α , and therefore Bry, surface brightness decreases with size ([Frew et al. 2016](#)), it follows that the average H₂ 1-0 S(1) / Bry surface brightness ratio increases with size and age. The trend between the 1-0 S(1) / Bry and 1-0 S(1) /

2-1 S(1) ratios has been investigated in [Marquez-Lugo et al. \(2015\)](#). We have taken fig. 7 from this work, included our data, and reproduced the graph here as Fig. 4b. Additional data comes from [Hora et al. \(1999\)](#), [Lumsden et al. \(2001\)](#), [García-Hernández et al. \(2002\)](#), [Davis et al. \(2003\)](#), [Likkell et al. \(2006\)](#) and [Marquez-Lugo et al. \(2015\)](#). This plot shows a loose positive correlation between the 1-0 S(1) / 2-1 S(1) and 1-0 S(1) / Bry ratios, and our data is no exception to this trend. Again, we separate our targets into W-BPNe and R-BPNe, and there is a clear separation between the two bipolar types, where W-BPNe have lower 1-0 S(1) / Bry ratios than the R-BPNe (mean values of 1.5 \pm 0.8 and 10.6 \pm 6.0

respectively). Fig. 4b may then suggest an evolutionary sequence, where bipolar PNe move to larger 1-0 S(1) / Br γ and 1-0 S(1) / 2-1 S(1) ratios as they evolve.

PN G050.5+00.0 has the lowest 1-0 S(1) / 2-1 S(1) and 1-0 S(1) / Br γ ratios in our sample, with values of 4.5 and 0.05 respectively in the central region. If PNe do generate higher line ratios as they evolve, this would mean that PN G050.5+00.0 is the youngest PN in our sample. It is likely that UV fluorescence is largely contributing to the excitation of H $_2$ here, in regions closer to the central star. Assuming a fluoresced gas, a 1-0 S(1) / 3-2 S(3) value of 16 for PN G050.5+00.0 could indicate a high FUV flux with a density $\geq 10^5$ cm $^{-3}$ (Burton et al. 1990). We find good evidence for fast outflows in the lobes of PN G050.5+00.0 (see Sec 4.1), which increase the chance of the H $_2$ being shock-excited. This is likely the reason behind the small increase of the 1-0 S(1) / 2-1 S(1) ratio to 5.8 in the lobes.

A few of our objects have had their distances estimated in previous works, including PN G050.5+00.0 (5.4 kpc; Ellsworth-Bowers et al. 2015), PN G057.9-00.7 and PN G062.7+00.0 (6.8 kpc and 6.1 kpc respectively; Ramos-Larios et al. 2017). The angular resolution of the UWISH2 survey is 0.2 arcsec pixel $^{-1}$, which converts to roughly 1000 to 1400 AU pixel $^{-1}$ for these three objects. Distances to the remaining objects could be estimated using the H α surface brightness - radius relation (Frew et al. 2016) for objects with H α (or even Br γ) imaging available, so long as the extinction could be accurately determined. It is likely that many of the objects in this study suffer significant extinction as they lie in the Galactic Plane, especially those with detected Br γ emission and no H α emission - large extinctions indicate they may be located at large distances. As Machado et al. (2015) have shown, the ability to resolve structures within PNe, such as knots and filaments, depends largely on the spatial resolution of the observations. The large distances, combined with generally small angular sizes, mean it is difficult to describe in detail the fine-scale structures of the objects in this study without access to higher resolution observations.

6 CONCLUSIONS

In this work, we have presented medium resolution, K-band spectra of a sample of 29 Galactic Plane objects, including 4 true, 2 likely, 1 possible and 22 candidate PNe, taken from the UWISH2 survey. The candidate PNe were selected on the basis of their morphologies, and lack of association with known star-forming regions. Evidence for ionized material, in the form of either Br γ emission in our spectra or H α emission in narrow-band surveys, is found in all but 2 of the targets. One of these, PN G020.8+00.4, is likely to be a pPN - at an earlier stage of evolution with a central star not yet hot enough to ionize its surrounding environment. PN G004.7-00.8 has mid-IR colours indicative of a YSO. 13 of the candidate PNe show no clear H α emission, however we detect Br γ emission in their spectra. These objects potentially contribute to the optically-obscured PN population, and their discovery clearly highlights the need for multi-wavelength studies of PNe, to accurately predict the number of PNe in the Milky Way.

We have used our spectra to calculate line ratios, which

have been used to constrain the mechanisms dominating the excitation of H $_2$. Most of our targets that we believe to be PNe are either R-BPNe (large ring structures) or W-BPNe (pinched waist), while the remaining 3 are considered to be elliptical. In agreement with previous studies, we find the former are predominantly thermally excited, while in the latter, UV fluorescence may have more influence. The link between line ratios and the spatial extent of ionized emission could mean that W-BPNe are younger objects, while the R-BPNe are more evolved, and an evolutionary scheme in which one class evolves into the other is worth further investigation. While long-slit spectroscopy is a useful tool for measuring line ratios with the advantage of spatial information in one dimension, more detailed spatial information can be achieved using integral field spectroscopy (IFS). This would allow excitation mechanisms to be inferred over the entire target, while comparing to the two-dimensional structure of the ionized region.

ACKNOWLEDGEMENTS

The authors would like to thank the referee A. Machado for his report, along with J. E. Drew and P. W. Lucas for discussions which helped improve the manuscript. A. M. Jones acknowledges support from the UK's Science and Technology Facilities Council (STFC) [grant number ST/K502029/1]. The William Herschel Telescope and its service programme are operated on the island of La Palma by the Isaac Newton Group of Telescopes in the Spanish Observatorio del Roque de los Muchachos of the Instituto de Astrofísica de Canarias. This research has made use of the HASH PN database at <http://hashpn.space>, and the SIMBAD database, operated at CDS, Strasbourg, France.

REFERENCES

- Acosta Pulido J. A., et al., 2003, The Newsletter of the Isaac Newton Group of Telescopes, **7**, 15
- Aleman I., Gruenwald R., 2011, *A&A*, **528**, A74
- Anderson L. D., Bania T. M., Balsa D. S., Rood R. T., 2011, *ApJS*, **194**, 32
- Astropy Collaboration et al., 2013, *A&A*, **558**, A33
- Black J. H., Dalgarno A., 1976, *ApJ*, **203**, 132
- Black J. H., van Dishoeck E. F., 1987, *ApJ*, **322**, 412
- Burton M. G., 1987, PhD thesis, University of Edinburgh
- Burton M. G., Hollenbach D. J., Tielens A. G. G. M., 1990, *ApJ*, **365**, 620
- Burton M. G., Hollenbach D. J., Tielens A. G. G., 1992, *ApJ*, **399**, 563
- Casali M. M., Eiroa C., 1996, *A&A*, **306**, 427
- Cohen M., Parker Q. A., Green A. J., Miszalski B., Frew D., Murphy T., 2011, *MNRAS*, **413**, 514
- Currie M. J., Berry D. S., Jenness T., Gibb A. G., Bell G. S., Draper P. W., 2014, in *Astronomical Data Analysis Software and Systems XXIII. Proceedings of a meeting held 29 September - 3 October 2013 at Waikoloa Beach Marriott, Hawaii, USA*. Edited by N. Manset and P. Forshay ASP conference series, vol. 485, 2014, p.391. p. 391
- Davis C. J., Smith M. D., Stern L., Kerr T. H., Chiar J. E., 2003, *MNRAS*, **344**, 262
- Drew J. E., et al., 2005, *MNRAS*, **362**, 753

- Ellsworth-Bowers T. P., Rosolowsky E., Glenn J., Ginsburg A., Evans II N. J., Battersby C., Shirley Y. L., Svoboda B., 2015, *ApJ*, **799**, 29
- Fang X., Zhang Y., Kwok S., Hsia C.-H., Chau W., Ramos-Larios G., Guerrero M. A., 2018, *ApJ*, **859**, 92
- Frew D. J., Parker Q. A., Bojičić I. S., 2016, *MNRAS*, **455**, 1459
- Froebrich D., et al., 2011, *MNRAS*, **413**, 480
- Froebrich D., et al., 2015, *MNRAS*, **454**, 2586
- García-Hernández D. A., Manchado A., García-Lario P., Domínguez-Tagle C., Conway G. M., Prada F., 2002, *A&A*, **387**, 955
- Gledhill T. M., Forde K. P., 2015, *MNRAS*, **447**, 1080
- Gledhill T. M., Froebrich D., Campbell-White J., Jones A. M., 2018, *MNRAS*,
- Guerrero M. A., Villaver E., Manchado A., Garcia-Lario P., Prada F., 2000, *ApJS*, **127**, 125
- Hoare M. G., et al., 2012, *PASP*, **124**, 939
- Hollenbach D., Natta A., 1995, *ApJ*, **455**, 133
- Hollenbach D. J., Shull J. M., 1977, *ApJ*, **216**, 419
- Hora J. L., Latter W. B., Deutsch L. K., 1999, *ApJS*, **124**, 195
- Jones E., Oliphant T., Peterson P., et al., 2001, SciPy: Open source scientific tools for Python, <http://www.scipy.org/>
- Kastner J. H., Gatley I., Merrill K. M., Probst R., Weintraub D., 1994, *ApJ*, **421**, 600
- Kerber F., Claeskens J.-F., 1997, *A&A*, **318**, 561
- Likkel L., Dinerstein H. L., Lester D. F., Kindt A., Bartig K., 2006, *AJ*, **131**, 1515
- Lucy L. B., 1974, *AJ*, **79**, 745
- Lumsden S. L., Puxley P. J., Hoare M. G., 2001, *MNRAS*, **328**, 419
- Manchado A., Guerrero M. A., Stanghellini L., Serra-Ricart M., 1996, The IAC morphological catalog of northern Galactic planetary nebulae
- Manchado A., et al., 2003, in Rodriguez Espinoza J. M., Garzon Lopez F., Melo Martin V., eds, Vol. 16, Revista Mexicana de Astronomia y Astrofisica Conference Series. pp 43–45
- Manchado A., Stanghellini L., Villaver E., García-Segura G., Shaw R. A., García-Hernández D. A., 2015, *ApJ*, **808**, 115
- Marquez-Lugo R. A., Ramos-Larios G., Guerrero M. A., Vázquez R., 2013, *MNRAS*, **429**, 973
- Marquez-Lugo R. A., Guerrero M. A., Ramos-Larios G., Miranda L. F., 2015, *MNRAS*, **453**, 1888
- Natta A., Hollenbach D., 1998, *A&A*, **337**, 517
- Paczyński B., 1970, *Acta Astronomica*, **20**, 47
- Parker Q. A., et al., 2005, *MNRAS*, **362**, 689
- Parker Q. A., et al., 2006, *MNRAS*, **373**, 79
- Parker Q. A., et al., 2012, *MNRAS*, **427**, 3016
- Parker Q. A., Bojičić I. S., Frew D. J., 2016, in *Journal of Physics Conference Series*. p. 032008 ([arXiv:1603.07042](https://arxiv.org/abs/1603.07042)), [doi:10.1088/1742-6596/728/3/032008](https://doi.org/10.1088/1742-6596/728/3/032008)
- Ramos-Larios G., Guerrero M. A., Sabin L., Santamaría E., 2017, *MNRAS*, **470**, 3707
- Reipurth B., Aspin C., 1997, *AJ*, **114**, 2700
- Richardson W. H., 1972, *J. Opt. Soc. Am.*, **62**, 55
- Robitaille T. P., et al., 2008, *AJ*, **136**, 2413
- Sternberg A., Dalgarno A., 1989, *ApJ*, **338**, 197
- Tielens A. G. G. M., Hollenbach D. J., 1993, in Weinberger R., Acker A., eds, *IAU Symposium Vol. 155, Planetary Nebulae*. p. 155
- Tody D., 1993, in Hanisch R. J., Brissenden R. J. V., Barnes J., eds, *Astronomical Society of the Pacific Conference Series Vol. 52, Astronomical Data Analysis Software and Systems II*. p. 173
- Treffers R. R., Fink U., Larson H. P., Gautier III T. N., 1976, *ApJ*, **209**, 793
- Urquhart J. S., et al., 2009, *A&A*, **501**, 539
- Zuckerman B., Gatley I., 1988, *ApJ*, **324**, 501

APPENDIX A: H₂ - K IMAGES**APPENDIX B: K-BAND SPECTRA****APPENDIX C: EMISSION LINE FLUXES**

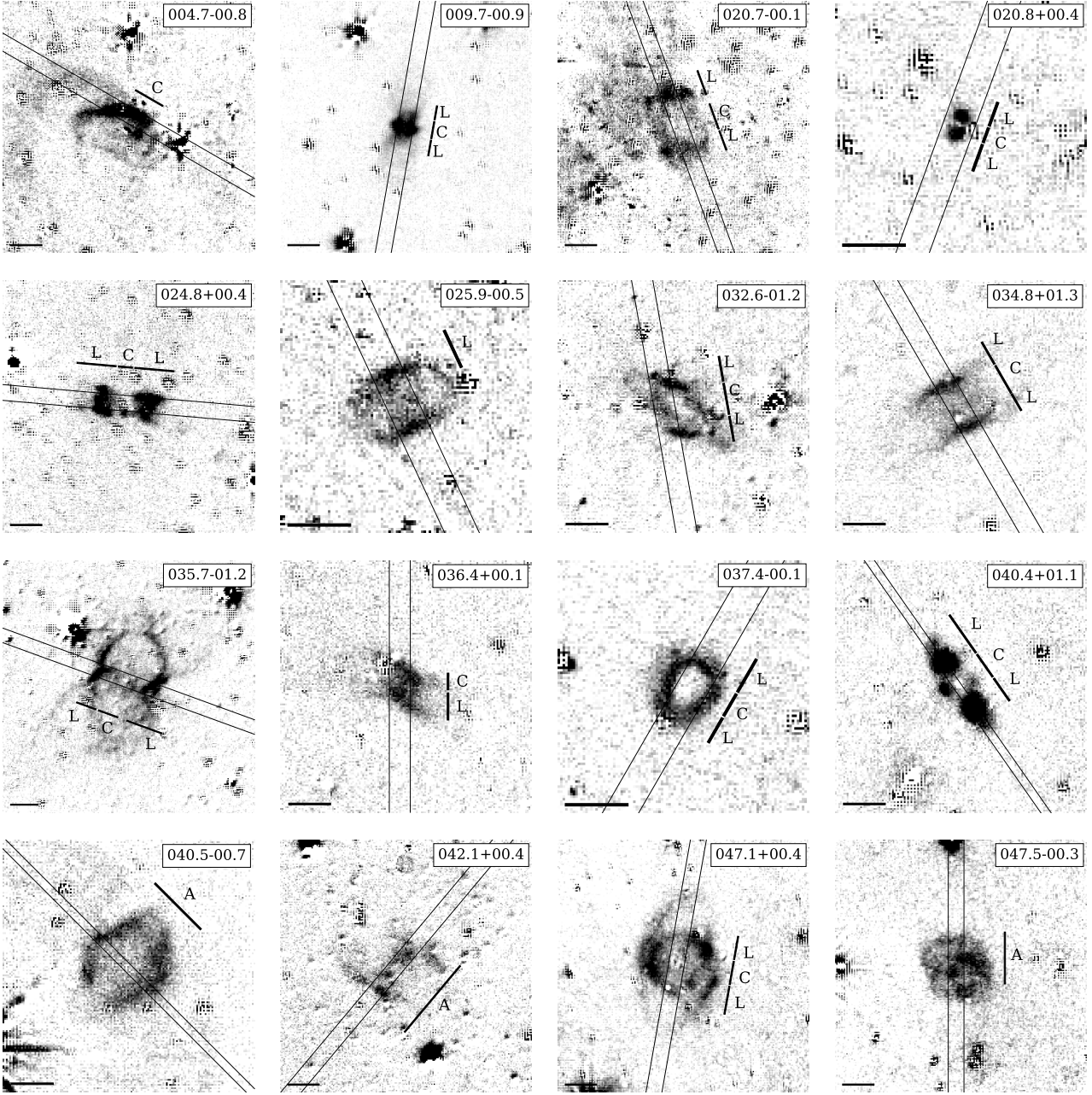


Figure A1. H_2 - K images taken from the UWISH2 survey, for targets PN G004.7-00.8 to G047.5-00.3, in order of increasing Galactic longitude. We overlay the LIRIS slit size and position, and the sections used for extraction - these are denoted 'C' for the centre, 'L' for a lobe and 'A' for all the target. The horizontal bar in the bottom left corner is a scale bar - representing 5 arcsec. In all figures, north is up, east is left.

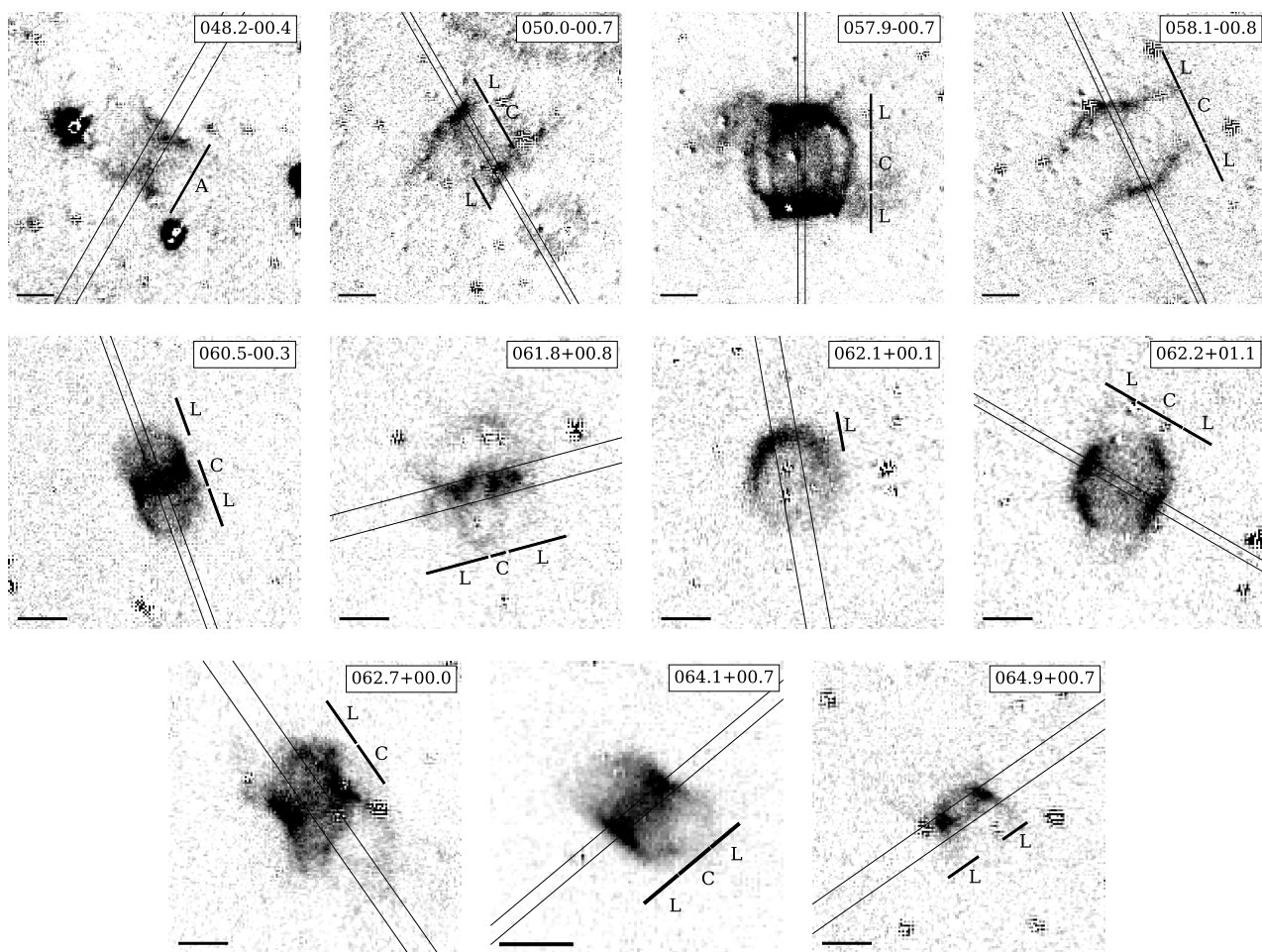


Figure A1. (cont.) $H_2 - K$ images for PN G048.2-00.4 to G064.9+00.7, excluding PN G050.5+00.0 and G059.7-00.8.

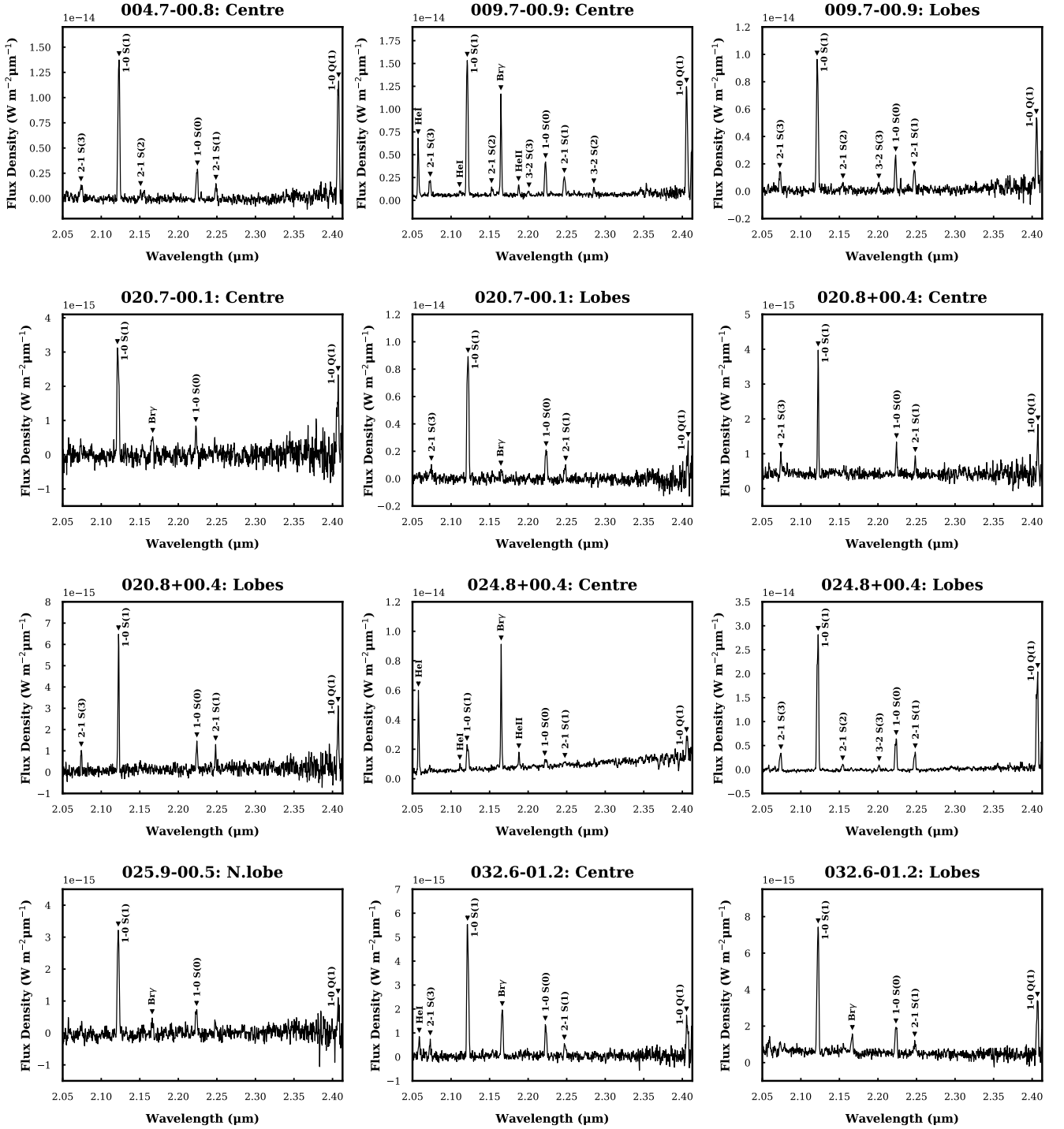


Figure B1. K-band spectra for targets PN G004.7-00.8 to G032.6-01.2, in order of increasing Galactic longitude. This includes spectra extracted from different regions of the same target, which are given in the title. We label any emission lines present.

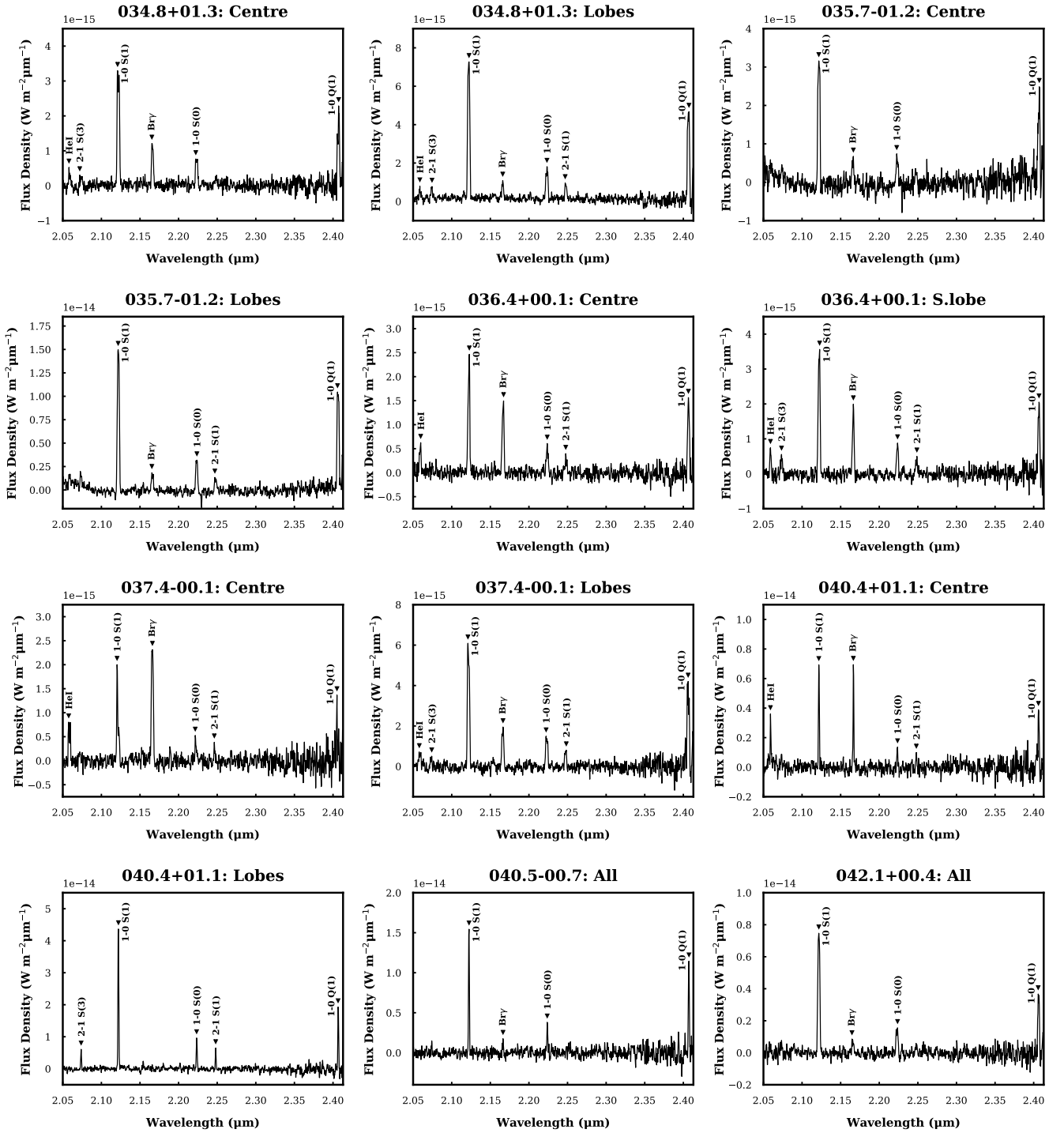


Figure B1. (cont.) Spectra for PN G034.8+01.3 to G042.1+00.4.

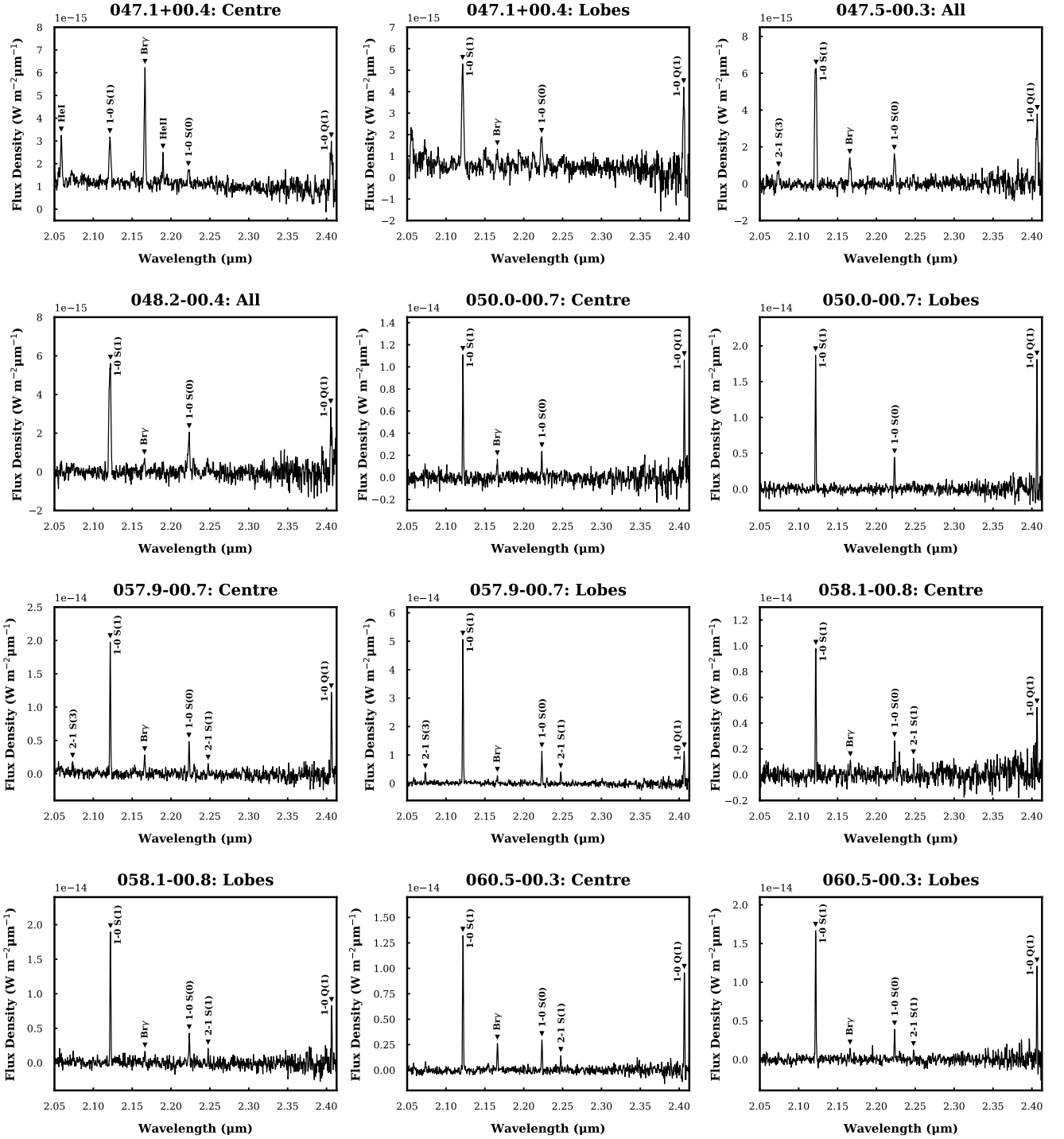


Figure B1. (cont.) Spectra for PN G047.1+00.4 to G060.5-00.3, excluding PN G050.5+00.0 and G059.7-00.8.

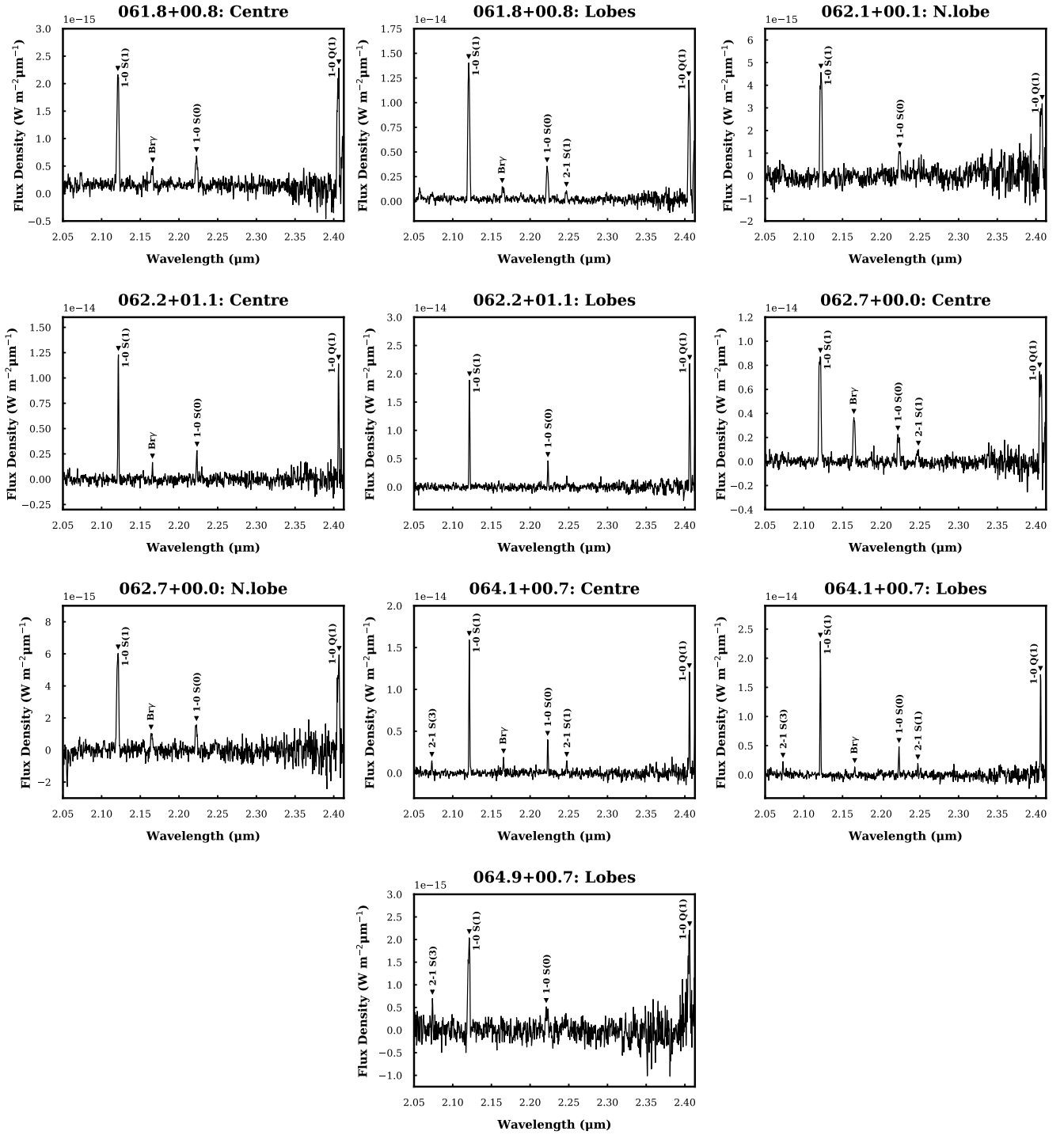


Figure B1. (cont.) Spectra for PN G061.8+00.8 to G064.9+00.7.

Table C1. Continuum-subtracted line fluxes and errors ($\times 10^{-19} \text{ Wm}^{-2}$) for K-band emission lines. Rest wavelengths of the emission lines are given in μm . Note these values are not corrected for extinction.

ID	Region	He I 2.0587	He I 2.1127	1-0 S(1) 2.1218	2-1 S(2) 2.1542	Bry 2.1661	He II 2.1891	3-2 S(3) 2.2014	1-0 S(0) 2.2233	2-1 S(1) 2.2477	3-2 S(2) 2.2870	1-0 Q(1) 2.4066
004.7-00.8	Centre	—	—	398 ± 22	17	—	—	—	78 ± 7	32 ± 5	—	343 ± 22
009.7-00.9	Centre	99 ± 6	9	412 ± 16	16 ± 3	169 ± 6	17 ± 2	7.6 ± 2.6	98 ± 5	56 ± 4	15 ± 3	332 ± 14
	Lobes	—	—	280 ± 10	11 ± 4	—	—	11 ± 3	59 ± 3	39 ± 4	—	147 ± 9
020.7-00.1	Centre	—	—	99 ± 7	—	16 ± 4	—	—	17 ± 2	—	—	59 ± 8
	Lobes	—	—	282 ± 17	—	15 ± 5	—	—	64 ± 5	25 ± 5	—	49 ± 14
020.8+00.4	Centre	—	—	56 ± 2	—	—	—	—	15 ± 1	7.9 ± 1.4	—	23 ± 3
	Lobes	—	—	104 ± 4	—	—	—	—	25 ± 2	17 ± 3	—	57 ± 6
024.8+00.4	Centre	78 ± 3	5.4 ± 0.9	57 ± 8	—	115 ± 3	13 ± 1	—	23 ± 6	10 ± 3	—	46 ± 7
	Lobes	—	—	805 ± 65	27 ± 5	—	—	19 ± 4	185 ± 15	94 ± 9	—	597 ± 51
025.9-00.5	North lobe	—	—	95 ± 5	—	8.6 ± 2.9	—	—	22 ± 2	—	—	23 ± 7
032.6-01.2	Centre	16 ± 3	—	155 ± 9	—	53 ± 2	—	—	34 ± 3	13 ± 2	—	44 ± 7
	Lobes	—	—	211 ± 12	—	28 ± 3	—	—	43 ± 4	15 ± 2	—	77 ± 8
034.8+01.3	Centre	8.7 ± 2.5	—	117 ± 12	—	34 ± 3	—	—	25 ± 3	—	—	61 ± 8
	Lobes	11 ± 3	—	234 ± 15	—	22 ± 3	—	—	50 ± 5	21 ± 2	—	140 ± 14
035.7-01.2	Centre	—	—	108 ± 10	—	17 ± 3	—	—	20 ± 2	—	—	69 ± 10
	Lobes	—	—	480 ± 28	—	53 ± 6	—	—	95 ± 8	40 ± 7	—	359 ± 27
036.4+00.1	Centre	14 ± 2	—	67 ± 5	—	42 ± 2	—	—	15 ± 2	10 ± 2	—	44 ± 4
	South lobe	15 ± 2	—	102 ± 7	—	47 ± 3	—	—	24 ± 3	12 ± 2	—	55 ± 6
037.4-00.1	Centre	21 ± 5	—	33 ± 5	—	75 ± 4	—	—	10 ± 2	5 ± 1	—	13 ± 4
	Lobes	15	—	199 ± 16	—	54 ± 4	—	—	49 ± 5	22 ± 4	—	130 ± 20
040.4+01.1	Centre	36 ± 7	—	99 ± 4	—	72 ± 4	—	—	20 ± 4	13 ± 4	—	67 ± 12
	Lobes	—	—	579 ± 12	—	—	—	—	135 ± 9	75 ± 6	—	228 ± 14
040.5-00.7	All	—	—	204 ± 5	—	21 ± 8	—	—	49 ± 9	—	—	171 ± 11
042.1+00.4	All	—	—	244 ± 12	—	21 ± 4	—	—	46 ± 7	—	—	92 ± 11
047.1+00.4	Centre	48 ± 6	—	61 ± 3	—	104 ± 3	21 ± 3	—	18 ± 3	—	—	43 ± 11
	Lobes	—	—	143 ± 5	—	16 ± 4	—	—	40 ± 5	—	—	75 ± 14
047.5-00.3	All	—	—	202 ± 13	—	37 ± 4	—	—	40 ± 3	—	—	100 ± 11
048.2-00.4	All	—	—	180 ± 14	—	15 ± 3	—	—	51 ± 5	—	—	60 ± 14
050.0-00.7	Centre	—	—	140 ± 6	—	23 ± 6	—	—	30 ± 4	—	—	123 ± 12
	Lobes	—	—	234 ± 6	—	—	—	—	62 ± 7	—	—	222 ± 18
050.5+00.0	Centre	1920 ± 30	212 ± 19	209 ± 9	—	3890 ± 80	93 ± 4	—	67 ± 8	46 ± 4	182 ± 7	175 ± 20
	Lobes	109 ± 10	15 ± 6	518 ± 15	28 ± 10	256 ± 9	—	32 ± 6	136 ± 10	89 ± 5	21 ± 7	364 ± 21
057.9-00.7	Centre	—	—	277 ± 8	—	43 ± 5	—	—	61 ± 6	20 ± 6	—	158 ± 13
	Lobes	—	—	669 ± 10	—	29 ± 9	—	—	141 ± 8	51 ± 6	—	148 ± 19
058.1-00.8	Centre	—	—	127 ± 7	—	16 ± 7	—	—	32 ± 6	—	—	64 ± 15
	Lobes	—	—	244 ± 6	—	24 ± 6	—	—	58 ± 7	18 ± 6	—	95 ± 15
059.7-00.8	Lobes	—	—	503 ± 8	—	59 ± 7	—	—	119 ± 7	38 ± 6	—	378 ± 14
060.5-00.3	Centre	—	—	177 ± 5	—	39 ± 2	—	—	40 ± 3	15 ± 3	—	121 ± 10
	Lobes	—	—	215 ± 7	—	18 ± 5	—	—	49 ± 4	16 ± 5	—	137 ± 13
061.8+00.8	Centre	—	—	61 ± 3	—	8.8 ± 1.5	—	—	15 ± 2	—	—	61 ± 8
	Lobes	—	—	409 ± 17	—	36 ± 8	—	—	107 ± 7	31 ± 5	—	327 ± 25
062.1+00.1	North lobe	—	—	145 ± 13	—	—	—	—	35 ± 4	—	—	103 ± 12
062.2+01.1	Centre	—	—	166 ± 4	—	14 ± 3	—	—	41 ± 5	—	—	148 ± 13
	Lobes	—	—	255 ± 4	—	—	—	—	55 ± 4	—	—	269 ± 15
062.7+00.0	Centre	—	—	309 ± 22	—	113 ± 8	—	—	67 ± 11	25 ± 6	—	244 ± 42
	North lobe	—	—	191 ± 11	—	30 ± 5	—	—	43 ± 5	—	—	168 ± 26
064.1+00.7	Centre	—	—	206 ± 6	—	23 ± 4	—	—	52 ± 4	22 ± 4	—	146 ± 10
	Lobes	—	—	282 ± 4	—	14 ± 4	—	—	64 ± 4	21 ± 6	—	204 ± 15
064.9+00.7	Lobes	—	—	58 ± 6	—	—	—	—	18 ± 4	—	—	65 ± 9

This paper has been typeset from a $\text{T}_{\text{E}}\text{X}/\text{L}^{\text{A}}\text{T}_{\text{E}}\text{X}$ file prepared by the author.